Indentation and Bifurcation of Inflated Membranes

Tianshu Liu[1*], Maurizio Chiaramonte[1], Amirhossein Amini[1], Yigit Menguc[1], G. M. Homsy[1,2]

[1]Facebook Reality Labs Research, Redmond, WA, 98052, USA

[2]University of Washington, WA, 98195, USA

[*] Corresponding author: Tianshu.liu@fb.com

Abstract: We study pneumatically inflated membranes indented by rigid indenters of different sizes and shapes. When the volume of the inflated membrane is beyond a critical value, a symmetric deformation mode becomes unstable and the system follows a path of asymmetric deformation. This bifurcation is analyzed analytically for a 2D membrane with either a line or plane indenter for which the stable deformation path is determined by computing the total system potential energy of different configurations. An axisymmetric membrane with indenters of different shapes and sizes is further investigated numerically. In this case, a cylindrical indenter can always trigger bifurcation while a small spherical indenter tends to be encapsulated rather than induce an asymmetric deformation mode. This result suggests that the observed bifurcation behavior can be actively tuned and even triggered selectively by tuning indenter shape and size. We also demonstrate the effects of friction and biased bifurcation analytically through the example of a 2D membrane with a line indenter.

1. Introduction

Inflation of soft and thin elastic materials is one of the most popular actuation technologies for driving modern soft robots [1], wearable haptic devices [2,3], and future space habitats [4] owing to the high energy density and uniformity of pneumatic forces [5]. The outer shell structure of such devices needs to be made of material that is highly stretchable or foldable such that it can be inflated with relatively low pressure while simultaneously exhibiting a large actuation stroke and safe interaction with potentially fragile environments such as humans [6,7]. The bending stiffness of the structure is often minimized to better adapt to unknown shapes of other structures that come into contact with the soft robots [8]. For these types of pneumatically powered devices, the outer soft-shell structures, which are typically thin, can be approximated as connected membranes. Therefore, many interactions between soft robots and environments and contact between wearable human computer interface (HCI) devices and human tissues can be treated as inflated membranes that are indented by indenters of various shapes. Accordingly, a systematic understanding of indentation of inflated membranes can potentially provide great insights into the designs and performance limits of soft robots.

The problem of indentation of inflated membranes naturally involves many sources of nonlinearity such as contact forces, large deformations, and nonlinear material constitutive behavior. Such nonlinearities can render the indentation process unstable and cause the deformation to deviate from its original and idealized path. In fact, our childhood experience of playing balloon stomp already suggests that when we put too much pressure on a balloon or when the balloon itself is too large, it is hard to keep the balloon right under one's foot, i.e., it tends to escape. Instability and bifurcation from stable and symmetric deformation paths often lead to loss of overall structure stiffness and should be avoided for load bearing applications [9]. For other applications, instabilities can be used as a switch [10] or even an actuator [11]. In any case, it is important to understand the bifurcation associated with indentation of inflated membranes in order to fully explore the design space of soft robots interacting with geometrically complex environments.

Previous studies for interfaces of droplets have already shown such instabilities. For example, compression of a droplet or capillary bridge between rigid surfaces will cause an axisymmetric droplet to become asymmetric [12]. A system of two droplets placed on top of one another and separated by an elastic membrane is also unstable, as a result, droplets tend to repel each other [13]. Both the inflated membrane and droplet systems can be seen as a class of problems in which isotropic hydrostatic pressure is in equilibrium with a surface that is in tension. However, replacement of a capillary surface of constant surface tension by an elastic membrane introduces new nonlinearities and makes the analysis of the indentation process more challenging. In fact, coupling of material nonlinearity with large deformation-induced curvature alone can produce many interesting bifurcation phenomena, e.g. localized bulging [14,15] and necking [16]. For hyper-elastic balloons, it is well known that pressure is normally not a monotonic function of membrane deformation, leading to a jump in deformation under pressure-controlled loading [17,18]. Because of a lack of bending stiffness, an inflated membrane is often wrinkled if coupled with flexible boundary conditions [19–21] and inflation of a wrinkled membrane can lead to non-trivial instabilities [22]. Including contact forces adds additional nonlinearities into the system. Contact studies for inflated membranes has been limited primarily to contact with a flat substrate [23–26] or a small indenter [27–30] and the associated instability behavior is limited to symmetric configurations [31].

In this work, we study indentation and bifurcation behavior of inflated membranes of different initial configurations. For simplicity, we assume that the indenters are rigid and contact between indenters and membranes is frictionless (although this is relaxed in a later section). The membrane is assumed to be a hyper-elastic material that supports general large deformations. Starting from 2D and cylindrical indenters, the critical condition for bifurcation can be determined analytically for two limiting cases, i.e., line contact and plane contact (indenters with radius equal to zero or infinity, respectively). Cases with finite radius cylindrical indenters are solved using finite element methods (FEMs). We then further consider contact between inflated axisymmetric membranes with cylindrical and spherical indenters of finite radius. In this case we find that bifurcation can be observed for cylindrical indenters but not for small spherical indenters, suggesting that it is possible to selectively trigger bifurcation of inflated membranes by using indenters of different sizes and shapes.

2. Mechanics of an Inflated Membrane

For soft robotic applications, the membrane often needs to go through fairly large deformation, with strains of the order of unity. By considering both finite amplitude contact and bifurcation there is no predetermined deformation pattern. Therefore, a general membrane model that allows arbitrarily large deformation should be used. Here, we follow the approach outlined by [32,33] in which the stress is uniform across the thickness of the membrane and a local plane-stress condition (i.e., stress component normal to the membrane is zero) is always satisfied.

Let $\Gamma_0 \in R^3$ denote the mid-surface of an undeformed membrane with thickness h_0 whose domain is defined as

$$\Omega_0 = \left\{ \mathbf{X} \middle| -h_0/2 < \phi(\mathbf{X}) < h_0/2 \right\}, \tag{1}$$

where $\phi: R^3 \to R$ is the signed distance function to the mid-surface Γ_0. Let $\boldsymbol{\varphi}: \Omega \to \Omega_t$ denote the deformation map. By making the kinematic assumption that plane sections remain plane and normal to the mid-surface, the deformation of the membrane can be expressed as:

$$\boldsymbol{\varphi}(\mathbf{X}) = \mathbf{x}\left(\mathbf{X}_{\Gamma_0}\right) + \phi(\mathbf{X})\mathbf{m}\left(\mathbf{X}_{\Gamma_0}\right), \tag{2}$$

where $\mathbf{m} = \lambda_3\mathbf{n}$, $\mathbf{n}$ is the unit normal to the mid surface of the membrane in the deformed configuration, which we denote by Γ_t, and λ_3 is the stretch ratio of the membrane in the thickness direction. With slight abuse of notation, let $\mathbf{X}(\xi^1,\xi^2)$, $\mathbf{X}:\hat{\Gamma} \to \Gamma_0$ be a parameterization of Γ_0. Similarly, let $\mathbf{x}(\xi^1,\xi^2)$, $\mathbf{x}:\hat{\Gamma} \to \Gamma_t$ be a parametrization of Γ_t such that we can define a set of induced bases to the tangent space of Γ_0 and Γ_t as:

$$\mathbf{G}_\alpha = \frac{\partial \mathbf{X}}{\partial \xi^\alpha}, \ \mathbf{g}_\alpha = \frac{\partial \mathbf{x}}{\partial \xi^\alpha}, \ \alpha = 1,2 \,. \tag{3}$$

Further we define $\mathbf{G}_3$ as the normal of the undeformed membrane, $\mathbf{g}_3 = \mathbf{m}$. Then the reciprocal basis $\mathbf{G}^i$ and $\mathbf{g}^i$ can be defined through the relation $\mathbf{G}^i \cdot \mathbf{G}_j = \delta^i_j$ and $\mathbf{g}^i \cdot \mathbf{g}_j = \delta^i_j$, where $i,j = 1,2,3$. Now the deformation gradient tensor can be evaluated as

$$\mathbf{F}\big|_{\Gamma_0} = \nabla_X \boldsymbol{\varphi}\big|_{\Gamma_0} = \frac{\partial \mathbf{x}}{\partial \xi^\alpha} \otimes \mathbf{G}^\alpha + \mathbf{m} \otimes \mathbf{N} = \mathbf{g}_i \otimes \mathbf{G}^i, \ \alpha = 1,2, \ i = 1,2,3 \,. \tag{4}$$

For all the examples in this work, we assume that the reference configuration of the membrane lies on a plane such that we can use constant orthogonal unit vectors $\mathbf{E}_\alpha = \mathbf{G}^\alpha = \mathbf{G}_\alpha$, $\alpha = 1,2$ as the basis and define the normal as $\mathbf{E}_3 = \mathbf{E}_1 \times \mathbf{E}_2$.

For a general hyper-elastic constitutive law, the Cauchy stress $\boldsymbol{\sigma}$ at the mid-surface of the membrane can be written as

$$\boldsymbol{\sigma}\big|_{\Gamma_0} = \frac{1}{J} \frac{\partial W(\mathbf{F}\big|_{\Gamma_0})}{\partial \mathbf{F}\big|_{\Gamma_0}} \mathbf{F}\big|_{\Gamma_0}^T \,, \tag{5}$$

where $W(\mathbf{F})$ is the strain energy density function and $J := \sqrt{\det(\mathbf{F}\mathbf{F}^T)}$. In this work, we demonstrate our results using an incompressible neo-Hookean model for simplicity, where $W(\mathbf{F}) = \frac{\mu}{2}(I_1(\mathbf{C}) - 3)$, μ is the shear modulus of the membrane and $I_1(\mathbf{C})$ is the first invariant of the right Cauchy-Green tensor $\mathbf{C} = \mathbf{F}^T\mathbf{F}$. Later, we will show that, at least for the 2-D scenario, most of our results are independent of the material model selection as long as the strain energy density function is a monotonic function of the stretch ratio. Using the plane stress condition (i.e., $\boldsymbol{\sigma} \cdot \mathbf{n} = \mathbf{0}$) [34], the Cauchy stress can be expressed as

$$\boldsymbol{\sigma}\big|_{\Gamma_0} = \mu \mathbf{F}\big|_{\Gamma_0} \mathbf{F}\big|_{\Gamma_0}^T - \mu\lambda_3^2 \mathbf{1} \,. \tag{6}$$

The total energy of an inflated membrane under volume control can be expressed as

$$\Pi(\boldsymbol{\varphi}, \lambda_P) = \int_\Omega W(\mathbf{F})dV - \lambda_P(V(\boldsymbol{\varphi}) - V_0) \,, \tag{7}$$

where $\boldsymbol{\varphi}$ is the displacement field defined in Eq. (2), $\lambda_P(V(\boldsymbol{\varphi}) - V_0)$ is the Lagrange multiplier term that constrains the volume of inflated membrane to be equal to a pre-specified value V_0. Using the variational principle, solving the problem of membrane inflation is equivalent to finding $\boldsymbol{\varphi} \in H$ and $\lambda_P \in R$ such that the variation of Π relative to $\boldsymbol{\varphi}$ and λ_P is zero,

$$\left\langle \delta\Pi, \{\delta\boldsymbol{\varphi}, \delta\lambda_P\} \right\rangle = 0, \ \forall \delta\phi \in TH, \ \delta\lambda_P \in R .$$

(8)

Here $\delta\boldsymbol{\varphi} \in TH, \delta\lambda_P \in R$ and H and TH are the sets of admissible solutions and variations, respectively. Substituting Eq. (4), (5) and (7) into (8) and assuming that the stress is a constant throughout the thickness, the strong form governing equations of the system can be obtained as

$$\begin{aligned} \nabla_S \cdot \boldsymbol{\tau} + P\mathbf{n} &= \mathbf{0} \\ P &= \lambda_P \\ V(\boldsymbol{\varphi}) &= V_0 \end{aligned} ,$$

(9)

where $\boldsymbol{\tau} := \lambda_3 h_0 \boldsymbol{\sigma}\big|_{\Gamma_0}$ is the membrane stress, $\nabla_S \cdot \boldsymbol{\tau} = \frac{\partial \boldsymbol{\tau}}{\partial \xi^\alpha} \cdot \mathbf{g}^\alpha$ is the surface divergence of $\boldsymbol{\tau}$ and P is the pressure applied on the membrane which numerically equal to the Lagrange multiplier λ_P. Note that $\boldsymbol{\tau}$ plays an analogous role to surface tension in the case of a droplet, and, with a suitable definition of $\boldsymbol{\tau}$, the first equation of (9) is equivalent to the Young-Laplace equation of capillary statics.

3. Indentation of a 2D membrane with a cylindrical indenter

As the simplest case, we consider a 2D membrane indented by a cylindrical indenter as shown in Figure 1. A membrane of width $2a$ is inflated by a uniform pressure and is in contact with a rigid cylinder of radius r_c. Both the cylindrical indenter and membrane are infinitely long in the out of plane direction (plane strain) and the distance between the undeformed membrane and the lower edge of the cylinder is d. The basis for the undeformed configuration is $\{\mathbf{E}_1, \mathbf{E}_2, \mathbf{E}_3\}$, as defined in section 2, and that for the deformed membrane is $\{\lambda\mathbf{e}_\xi, \frac{1}{\lambda}\mathbf{e}_n, \mathbf{E}_2\}$, where $\mathbf{e}_\xi, \mathbf{e}_n$ are the unit tangent and unit normal in the deformed configuration as shown in Figure 1. λ is the in-plane stretch ratio of the membrane. Owing to material incompressibility, the stretch ratio in the thickness direction is $\lambda_3 = \frac{1}{\lambda}$. Then, following Eq. (4), the deformation gradient tensor can be written as

$$\mathbf{F} = \lambda\mathbf{e}_\xi\mathbf{E}_1 + \frac{1}{\lambda}\mathbf{e}_n\mathbf{E}_3 + \mathbf{E}_2\mathbf{E}_2 .$$

(10)

Substituting Eq. (10) into Eq. (6), the Cauchy membrane stress can be written as

$$\boldsymbol{\tau} = \frac{h_0}{\lambda}\boldsymbol{\sigma} = \mu h_0 \left(\lambda - \frac{1}{\lambda^3} \right)\mathbf{e}_\xi\mathbf{e}_\xi + \mu h_0 \left(\frac{1}{\lambda} - \frac{1}{\lambda^3} \right)\mathbf{E}_2\mathbf{E}_2 .$$

(11)

Therefore, the in-plane tension of the membrane is $T = \mu h_0 \left(\lambda - \frac{1}{\lambda^3} \right)$. Further substitution of Eq. (11) into the first equation of (9) yields

$$\begin{aligned} \frac{d\lambda}{d\xi} &= 0 \\ T\kappa &= P \end{aligned} ,$$

(12)

where the geometric condition $d\mathbf{e_\xi}/d\xi = -\kappa\mathbf{e_n}$ has been used and where κ is the curvature of the deformed membrane. From Eq. (12), it is clear that the shape of membrane that is not in contact with the indenter is part of a circle whose radius is determined by the balance of membrane tension and pressure. As shown in Figure 1, we denote the radius of the deformed membrane as r_m.
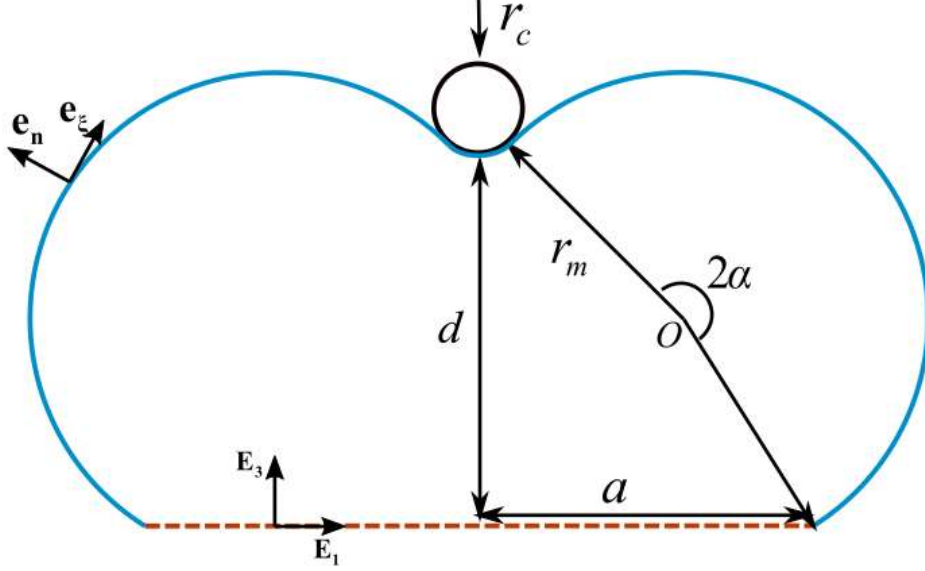

Figure 1 Schematics of an inflated 2D membrane indented by a rigid cylinder. The undeformed membrane is flat, represented by the dashed orange line, and the deformed membrane is denoted by the solid blue line.

We assume that the contact between the membrane and the indenter is frictionless and adhesionless so that the membrane is tangent to the indenter and the tensions in the membrane to the left and right of the indenter are equal. Since the pressure is also uniform, the radius of the left and right circles should also be equal.

3.1 Limiting case 1: line indentation ($r_c \to 0$)

We first consider the extreme case when the size of the indenter goes to zero, i.e., line indentation. As analyzed above, the cross-sectional deformed shape of membrane should be two parts of a single circle joined together at the point of indentation as shown in Figure 2. Denoting the smaller part of a circle as A and the larger part as B, there are three possible deformed configurations, i.e., A-A, B-B, or A-B. During a quasi-static indentation/inflation process, the system will prefer the configuration that has the lowest total energy.
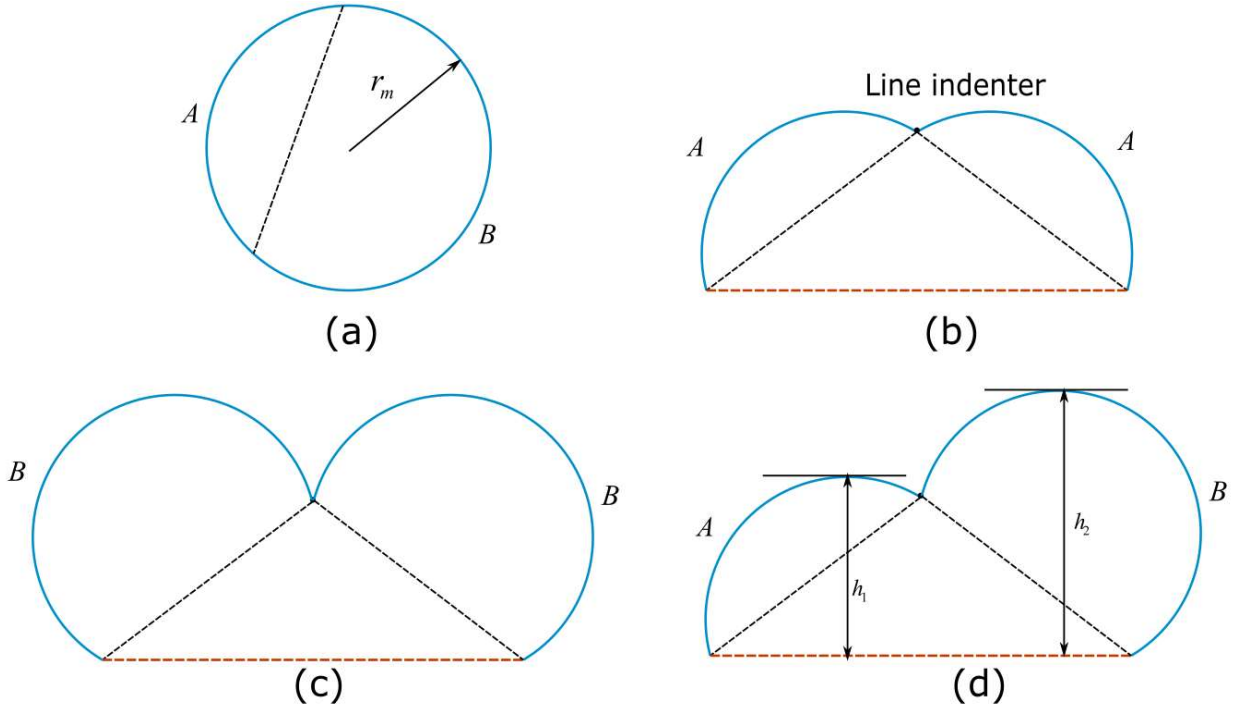
Figure 2 Schematics of the possible deformed shapes of an inflated 2D membrane under line indentation. (a) The shape of the inflated membrane has to be part of a circle with fixed radius and arclength, i.e. either part A or part B. (b) The two parts of the inflated membrane can be both part A or (c) both part B or (d) one part A and the other part B.

The loading process has many possible paths, such as pressure- or volume-controlled inflation while the indenter position remains fixed, or moving the indenter down (reducing d) while the pressure or volume remains fixed. Since we consider the indentation process as quasi-static and assume that contact between the indenter and membrane is frictionless, the system is conservative. Therefore, the solution is the same for all loading paths. Here, without loss of generality, we consider volume-controlled inflation of the membrane with a fixed indenter position.

The total volume, V (area in the case of a 2D system) enclosed by the membrane is the sum of the areas of the circular and triangular parts (see Figure 2). If the deformed configuration is symmetric, i.e., A-A or B-B type,

$$V = 2r_m^2 \left(\alpha - \sin\alpha\cos\alpha\right) + da ; \tag{13}$$

And the associated geometry relation is

$$r_m \sin\alpha = \frac{1}{2}\sqrt{a^2 + d^2} . \tag{14}$$

If the deformed configuration is asymmetric, i.e., A-B type, then:

$$V = \pi r_m^2 + ad . \tag{15}$$

Using the half-width of the undeformed membrane as the characteristic length, Eq. (13)-(15) can be normalized as

$$\overline{V} := \frac{V}{a^2} = 2\overline{r}_m^2 (\alpha - \sin\alpha\cos\alpha) + \overline{d} \qquad \text{or} \qquad \overline{V} = \pi\overline{r}_m^2 + \overline{d}$$

$$\overline{r}_m \sin\alpha = \frac{1}{2}\sqrt{1+\overline{d}^2}$$

(16)

where $\overline{r}_m = \dfrac{r_m}{a}$, $\overline{d} = \dfrac{d}{a}$. For an asymmetric deformed configuration, due to geometry constraints, it is necessary to have $\overline{r}_m \geq \dfrac{1}{2}\sqrt{1+\overline{d}^2}$. Therefore, a solution only exists when

$$\overline{V} \geq \frac{\pi}{4}\left(1+\overline{d}^2\right) + \overline{d} .$$

(17)

The in-plane stretch ratio of the membrane can be calculated as the ratio of the arclength of the deformed membrane to the initial membrane width $2a$,

$$\text{Symmetric: } \lambda = 2\alpha\overline{r}_m, \qquad \text{Asymmetric: } \lambda = \pi\overline{r}_m$$

(18)

Finally, the total energy of the system is simply the total elastic energy of the membrane, as we consider volume-controlled inflation with a fixed indenter position. Therefore, half of the total energy (we divide the energy by a factor of 2 for simplicity of expression) can be calculated as:

$$\overline{E} := \frac{E}{\mu h_0 a} = \lambda^2 + \frac{1}{\lambda^2} - 2 .$$

(19)

By solving Eq. (16) and substituting solutions to Eq. (18) and (19), we obtain the system energy for each type of solution as a function of volume. From there, we can determine which type of solution has the lower energy and how the shape of the membrane evolves as the volume increases. As an example, we set $\overline{d} = 0.5$ and the results are shown in Figure 3.
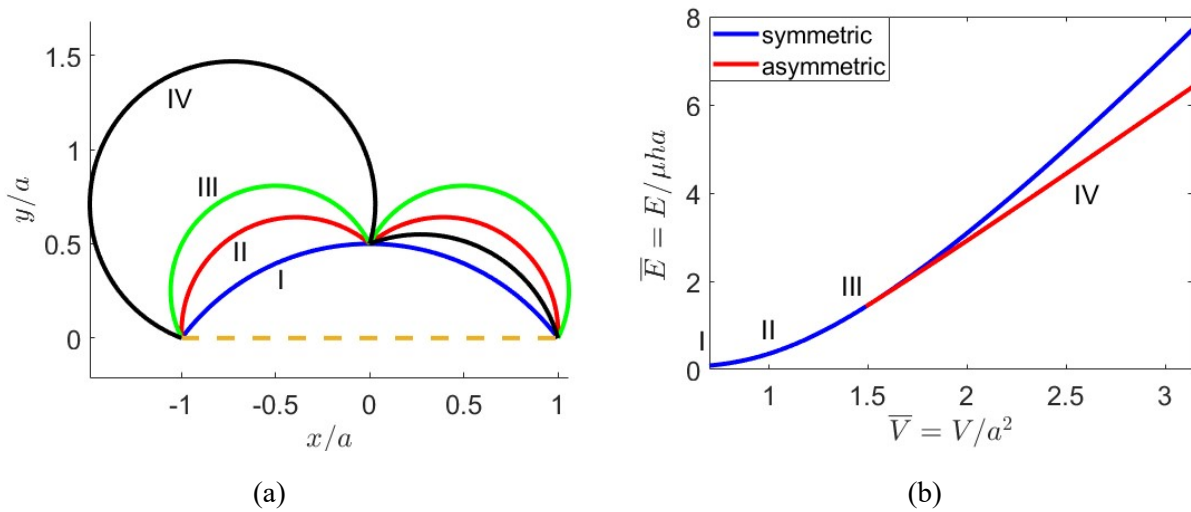

(a)

(b)

Figure 3 (a) Deformed membrane configuration for a line indenter as the volume gradually increases; (b) total energy of the system for the symmetric and asymmetric configurations as volume increases

As shown in Figure 3, when the membrane is inflated to configuration I, the membrane just makes contact with the indenter. At this point, the total volume enclosed by the deformed configuration has not reached the threshold given by Eq. (17). Hence, the only possible solution is the symmetric solution. As the volume increases, the membrane continues to be symmetrically stretched until configuration III is reached, at which point the volume condition for asymmetric solutions (17) is just met. Beyond configuration III, not only does the asymmetric solution exist but the total system energy is lower than that of the symmetric solution. This result indicates that, compared with the symmetric solution, the asymmetric configuration can reach the same volume with less membrane stretch and hence is energetically preferred. Therefore, the deformed membrane will follow the asymmetric deformation branch beyond configuration III, such as the shape given by configuration IV. Since the asymmetric configuration always has a lower energy, the critical volume of instability is the same as the condition for the asymmetric solution to exist, i.e.:

$$\overline{V}_C = \frac{\pi}{4}\left(1+\overline{d}^2\right)+\overline{d} .$$
(20)

Note that this condition is a pure geometry condition, so it is material independent.

The transition from the symmetric to the asymmetric configuration is a typical supercritical pitchfork bifurcation. To better visualize this, we choose the difference between the left and right part membrane height $\Delta h = h_1 - h_2$ (see Figure 2) as a signed quantity and a metric for measuring the degree of symmetry. Then the bifurcation diagram can be plotted as in Figure 4.
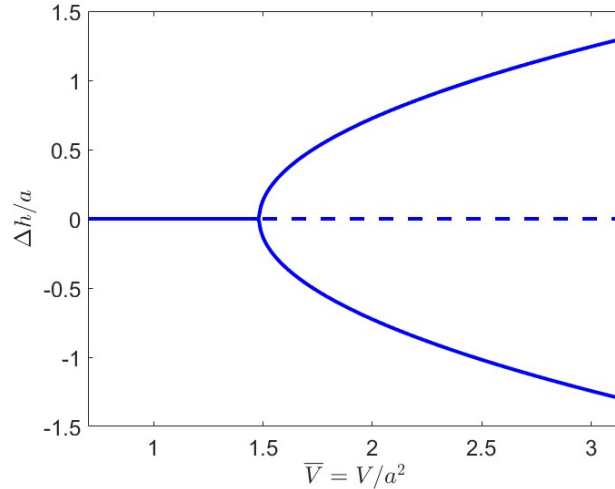

Figure 4 Bifurcation diagram for indentation of an inflated 2D membrane with a line indenter

3.2 Limiting case 2: Plane indentation ($r_c \rightarrow \infty$)

Here, we consider the other extreme limit in which the size of the indenter is infinitely large such that it becomes a plane indenter. As we assume frictionless and adhesionless contact between the membrane and indenter, the deformed membrane needs to be tangent to the plane indenter as shown in Figure 5.
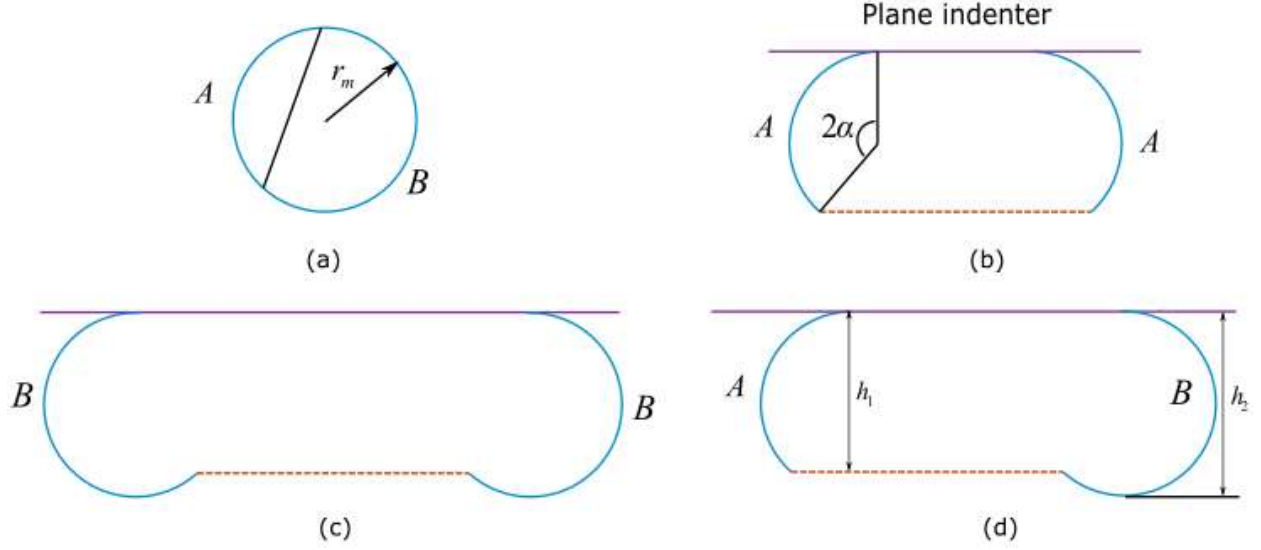
Figure 5 Schematics of the possible deformed shapes of an inflated 2D membrane under plane indentation. (a) The two arc parts of the inflated membrane have to be part of a circle with fixed radius and arclength, i.e. either part A or part B. (b) The two arc parts of the inflated membrane can be both part A or (c) both part B or (d) one part A and the other part B.

The analysis process is almost identical to the line indentation case. The governing equations can be determined through volume conservation, the tangent condition between the membrane and indenter at the point of contact, and the fixed boundary condition:

$$\overline{V} = 2\overline{r}_m^{\,2}\left(\alpha - \sin\alpha\cos\alpha\right) + \frac{1}{2}\left(2 + \overline{L}\right)\overline{d} \qquad\qquad \overline{V} = \pi\overline{r}_m^{\,2} + \frac{1}{2}\left(2 + \overline{L}\right)\overline{d}$$

symmetric:
$$\overline{r}_m\left(1 - \cos 2\alpha\right) = \overline{d} \qquad\qquad \text{asymmetric:} \quad \overline{r}_m\left(1 - \cos 2\alpha\right) = \overline{d} \qquad (21)$$
$$2\overline{r}_m\sin 2\alpha + \overline{L} = 2 \qquad\qquad\qquad\qquad \overline{L} = 2$$

where $\overline{L} := \dfrac{L}{a}$ is the normalized contact length. For an asymmetric configuration to exist, $\overline{r}_m$ should be at least $\dfrac{\overline{d}}{2}$, which means that the critical volume condition is

$$\overline{V} \geq \frac{1}{4}\pi\overline{d}^{\,2} + 2\overline{d}\,. \qquad (22)$$

The stretch ratio of the membrane is

$$\text{Symmetric: } \lambda = 2\alpha\overline{r}_m + \frac{1}{2}\overline{L}, \qquad \text{Asymmetric: } \lambda = \pi\overline{r}_m + 1\,. \qquad (23)$$
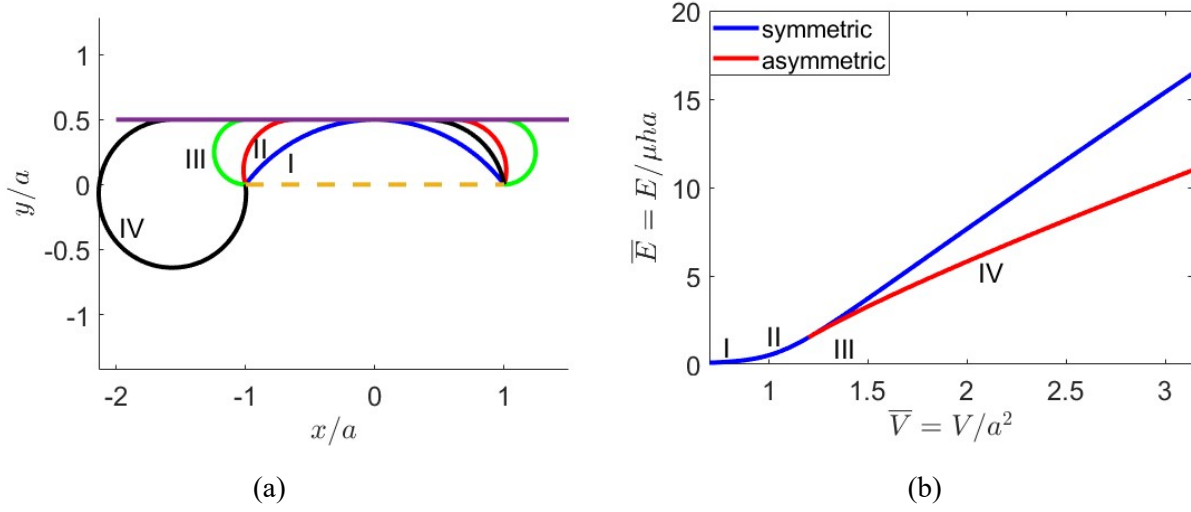
Figure 6 (a) Deformed membrane configuration for the plane indenter as the volume gradually increases (b) total energy of the system for the symmetric and asymmetric configurations as volume increases.

Setting $\bar{d} = 0.5$, the deformed shape can be determined by solving Eq. (21) and total energy can be calculated using Eq. (19). The results are given in Figure 6. This suggests that simply increasing the indenter contact area does not necessarily lead to a more stable indentation. In fact, indentation of inflated 2D membrane by a plane indenter still undergoes a supercritical pitchfork bifurcation process and the bifurcation diagram shows that the bifurcation happens at a lower volume compared to a line indenter (see Figure 7). Note that in contrast to typical pitchfork bifurcation, the bifurcation slope $d\overline{\Delta h} / d\overline{V}$ at the critical volume is finite. Beyond the critical volume, the contact from indenter limits the direction that the membrane can expand and the growth of $\overline{\Delta h}$ is simply equal to the growth of diameter. Therefore,

$$d\overline{\Delta h} / d\overline{V} \sim \frac{2d\overline{r_m}}{2\pi \overline{r_m} d\overline{r_m}} = \frac{1}{\pi \overline{r_m}} < \infty \,.$$
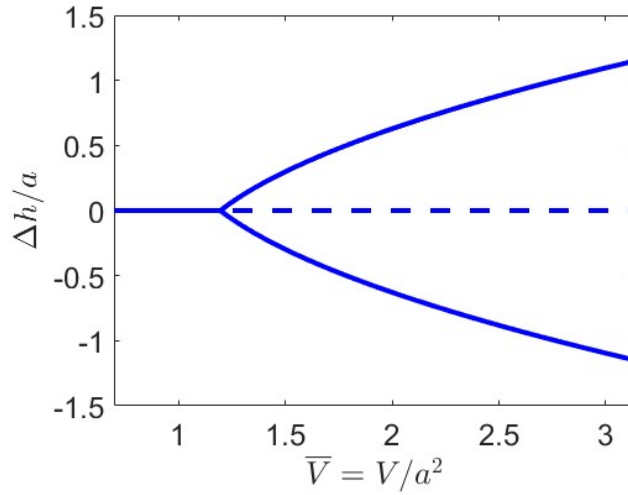

Figure 7 Bifurcation diagram for the indentation of an inflated 2D membrane with a plane indenter

3.3 Indenter with finite radius ($0 < r_c < \infty$)

We now consider the general case in which the cylindrical indenter has a finite radius. While it is possible to analytically derive the geometric and volume constraints, the process is tedious, and a broader goal of this work is to facilitate access to engineering tools in geometrically generalizable design. Here, we directly implement the variational formulation of the problem, i.e., Eq. (8), in the open-source finite element tool FEniCS. The numerical solutions are validated against the analytical solution for simple membrane inflation and has an error of less than 2%, as shown in Figure 8(a). We also performed a mesh convergence study, as shown in Figure 8(b), to ensure accurate results.

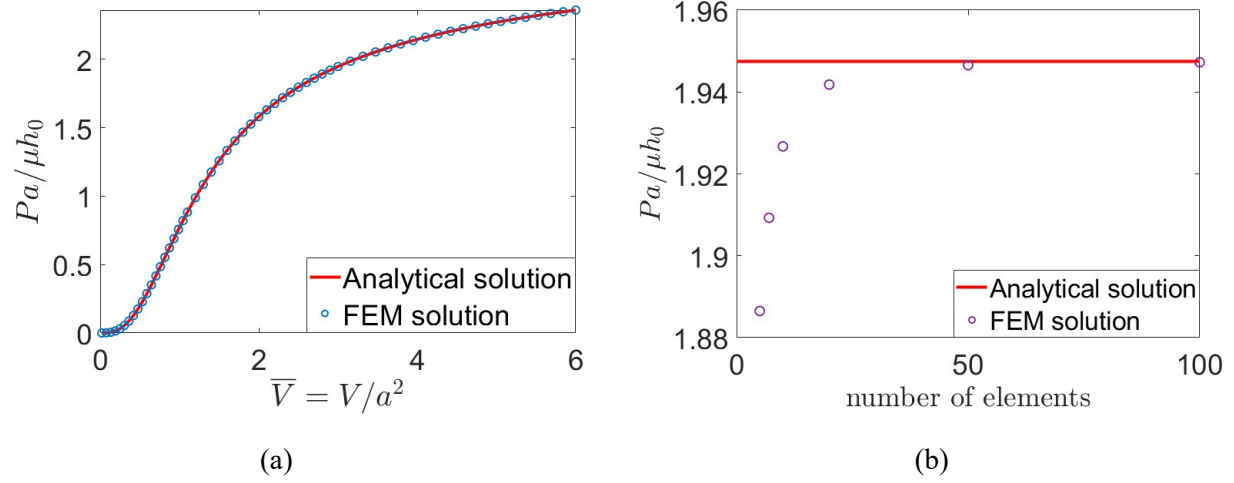(a)   (b)

Figure 8 Verification of FEM implementation (a) Verification against analytical solution (b) an example of mesh convergence test where pressure solution at $\overline{V} = 3.0$ is compared with analytical solution.

The contact between the indenter and the membrane can be implemented using a standard penalty approach. An example solution for an indenter with $\overline{r_C} = 0.2$ is given in Figure 9. Boundaries 1 and 2 of the membrane are fixed and boundaries 3 and 4 are fixed only in the y direction such that the membrane is in plane strain. Deformed membrane shapes before and after bifurcation are shown in Figure 9(b). Note that, to observe the bifurcation, a slight perturbation in cylinder position $\overline{\Delta x_C} = \dfrac{\Delta x_C}{a} = 10^{-5}$ is applied. The full process of inflation, contact, and bifurcation is shown in supplementary video S1.
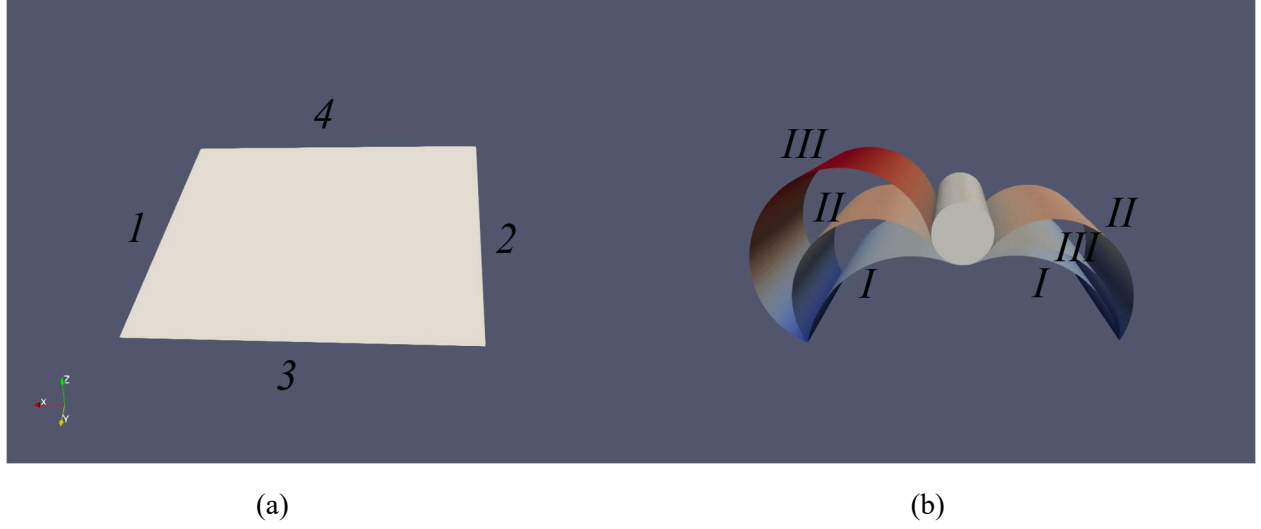
Figure 9 (a) Undeformed membrane shape. (b) Deformed membrane shape before bifurcation (I), at critical volume (II) and after bifurcation (III)

The bifurcation diagrams for different indenter sizes are given in Figure 10. As the radius of the indenter decreases, the critical volume approaches that for the line indentation case; on the other hand, as the radius of the indenter increases, the critical volume converges to the plane indentation result, which further verifies our numerical implementation. Our results also suggest that, as the indenter size increases, the critical volume where the bifurcation starts becomes smaller and the bifurcation slope $\dfrac{d\,\overline{\Delta h}}{d\overline{V}}$ changes from ∞ for the line indentation case to a finite value for the plane indentation case.
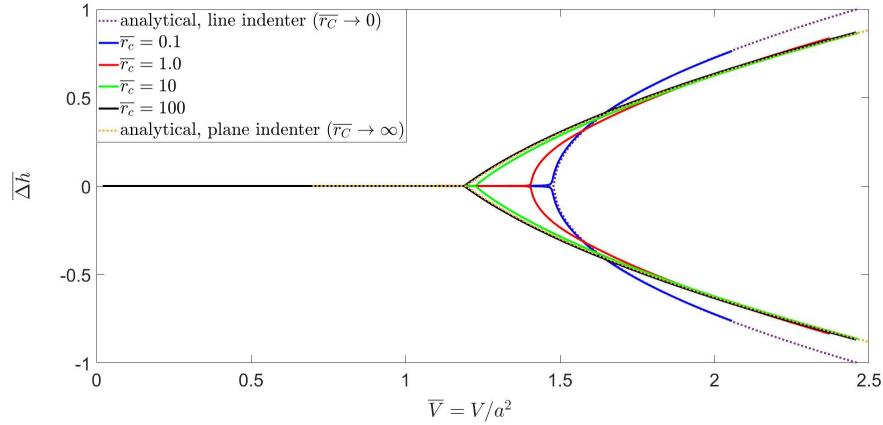

Figure 10 Bifurcation diagram for a cylindrical indenter with finite radius. When the indenter radius approaches to zero relative to the membrane width, the solution approaches the analytical result with the line indenter; similarly, when the indenter size relative to the membrane width approaches infinity, the solution approaches the analytical solution for the plane indenter.

3.4 Material model dependency

For 2D membrane and frictionless contact, the deformed membrane shape must be part of a circle and the stretch ratio is a constant for the entire membrane. Therefore, for any given volume, the deformed shape and stretch ratio can be determined purely based on geometry, as shown in Eq. (16) or Eq. (21) and Eq. (18) or Eq. (23). Figure 11 suggests that the stretch ratio for asymmetric deformation is always less than the

stretch ratio for symmetric deformation at any volume above the critical volume $\overline{V_C}$. Note that this conclusion is independent of material model selection. Therefore, as long as the strain energy density function is a monotonic function of the stretch ratio, the total energy for the asymmetric deformation mode is always less than the symmetric deformation mode. Our conclusion that the membrane bifurcation happens at $\overline{V_C}$ and follows the asymmetric deformation mode is material model independent. Note that even the post-buckling path as described by the $\overline{V} - \overline{\Delta h}$ plot (e.g., Figure 3(a), Figure 4, Figure 6(a) and Figure 7) is also material model independent as $\overline{\Delta h}$ is determined by geometry only as well. However, the difference in the total energy between the symmetric and the asymmetric deformation modes as well as the depths of the post-bucking energy wells do change with the constitutive law, consistent with previous studies [35].
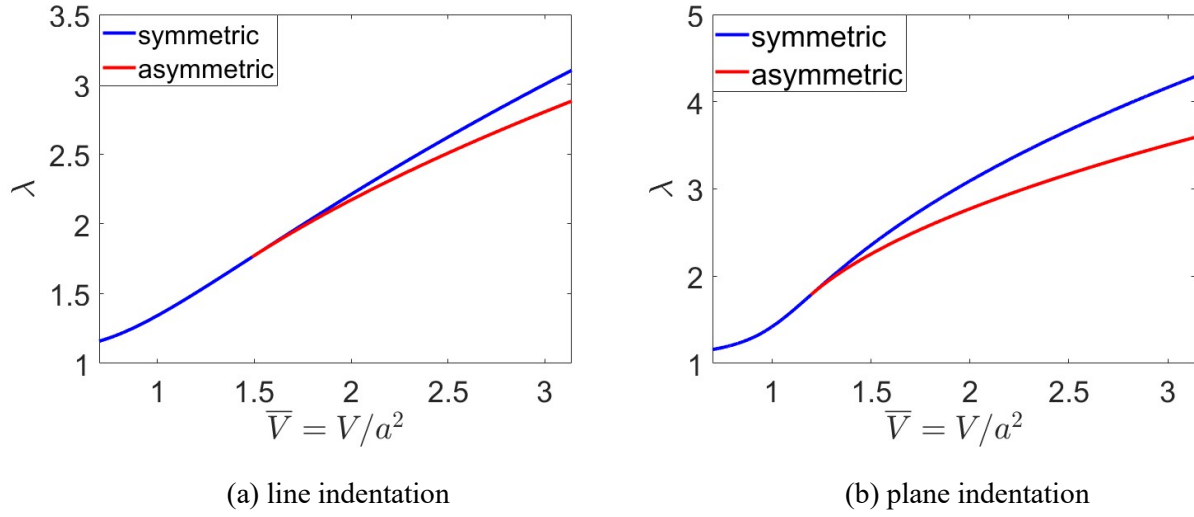

(a) line indentation   (b) plane indentation

Figure 11 stretch ratio as a function of normalized volume for (a) line indentation (b) plane indentation

4. Effects of membrane and indenter shape

With the numerical method introduced in section 3.3, we are well equipped to consider arbitrary membrane and indenter shapes. Here, we present our numerical results for an axisymmetric membrane in contact with i) a cylindrical and ii) a spherical indenter. For each indenter, we provide bifurcation results for different values of indenter radius.
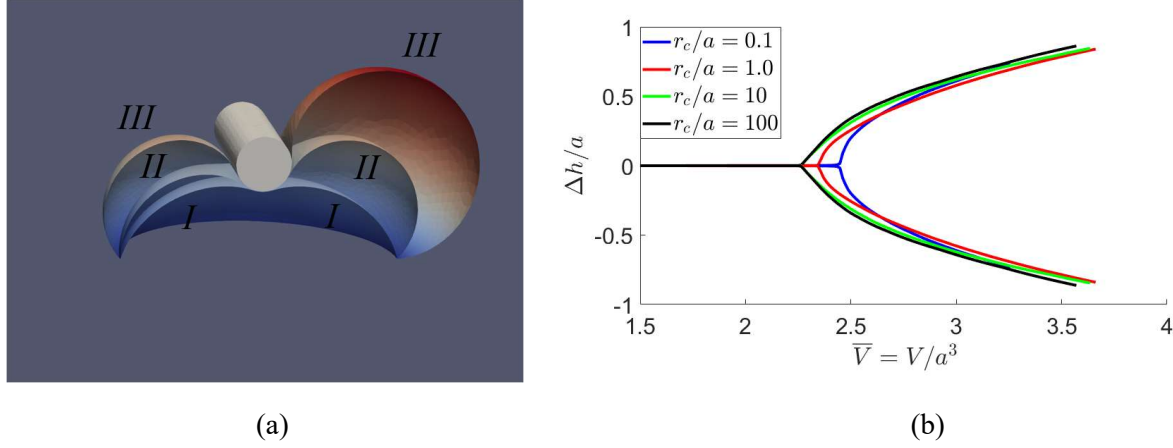
Figure 12 (a) cross-section of a deformed shape of an inflated membrane indented by a cylindrical indenter with radius $r_C/a = 0.2$. Three different cases shown include (I) volume is small such that membrane deformation is symmetric (II) bifurcation occurs and the right half become slightly bigger than the left half (III) The right half become significantly larger (b) Bifurcation diagrams for different indenter radii.

We first consider a circular membrane with a fixed boundary in contact with a cylindrical indenter. As shown in Figure 12 and supplementary video S2, the membrane bifurcates to an asymmetric configuration after a critical volume is reached, similar to the 2D case. Both the critical volume for bifurcation and bifurcation slope $\dfrac{d\,\overline{\Delta h}}{d\overline{V}}$ decrease as the size of the indenter increases, which again suggests that a larger indenter tends to make it easier for an inflated membrane to bifurcate.

Next, we replace the cylindrical indenter with a spherical indenter. As shown in Figure 13 and supplementary video S3, when the spherical indenter is small enough, it cannot excite a new mode of deformation that has less energy, and hence the symmetric state is the only stable one. The membrane tends to wrap around the sphere instead of being pushed to one side. Note that our simulation stops when the membrane right under the spherical indenter is so stretched that the size of deformed mesh is of the same order of indenter size such that contact between the membrane and the indenter cannot be maintained. At this point, the local stretch ratio of membrane is beyond 50 and it is likely that some material failure such as plastic deformation or local fracture would have already occurred. This result suggests that, for a small/sharp indenter, the membrane will be pierced through instead of pushed sideways, which is consistent with previous studies [36]. On the other hand, when the size of the spherical indenter increases to the same order of or even larger than the membrane dimension itself, the contact approaches the plane indentation limit and bifurcation will again occur (see supplementary video S4 for the case $r_S/a = 100$).
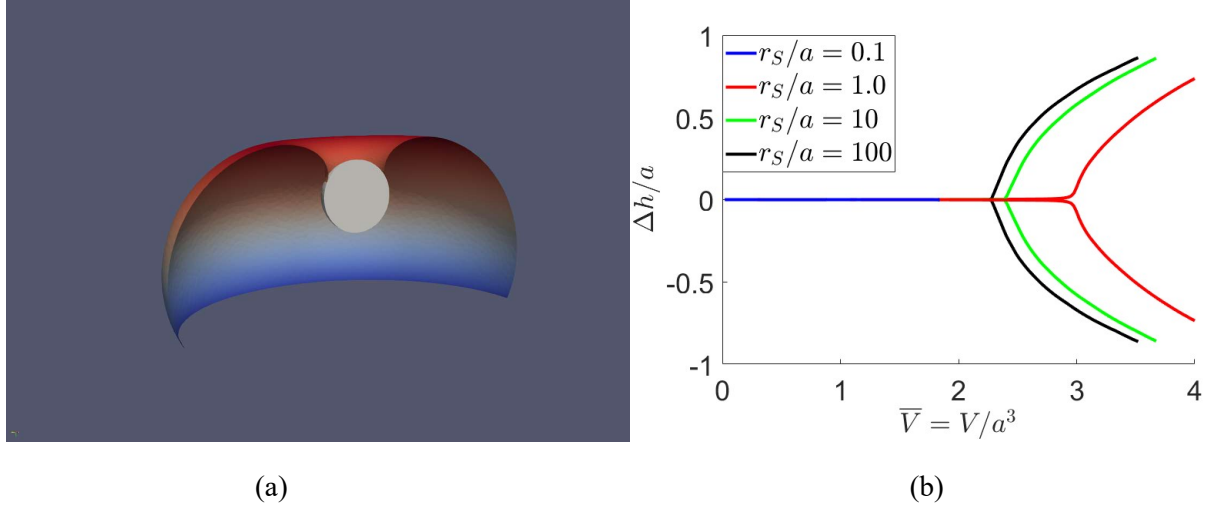
Figure 13 (a) cross-section of the deformed shape of an inflated membrane indented by a spherical indenter with radius $r_C / a = 0.2$. (b) bifurcation diagrams for different indenter radii.

For an axisymmetric membrane, the deformation involves stretch in both the radial and circumferential directions. Therefore, unlike the 2D scenario, the deformed shape may have some level dependency on the material model selection and so is the critical volume and the post-buckling path (e.g. Figure 13(b)). Such a dependency is beyond the scope of this work and can be pursued in a future work.

5. Biased bifurcation and the effects of friction

In this section, we demonstrate biased bifurcation and the effects of friction using a 2D membrane in contact with a line indenter as an example.

For an ideal system that has no perturbation or bias at all, the symmetric deformation is always a valid equilibrium solution and bifurcation would not occur. For frictionless contact, any infinitesimal bias such as putting the indenter slightly off center or even numerical error, is sufficient to trigger the bifurcation. If the geometry imperfection is finite as shown in Figure 14 (a), the symmetry of bifurcation no longer holds as the arclengths CP and CQ are not equal. Using the same geometry methods as given in Section 3.1, we get the bifurcation diagram shown in Figure 14 (b). The bifurcation paths disconnect into two pieces. Without perturbation, the membrane just follows the lower path. To access the upper branches, a rather large disturbance is required to overcome the energy barrier between the branches.
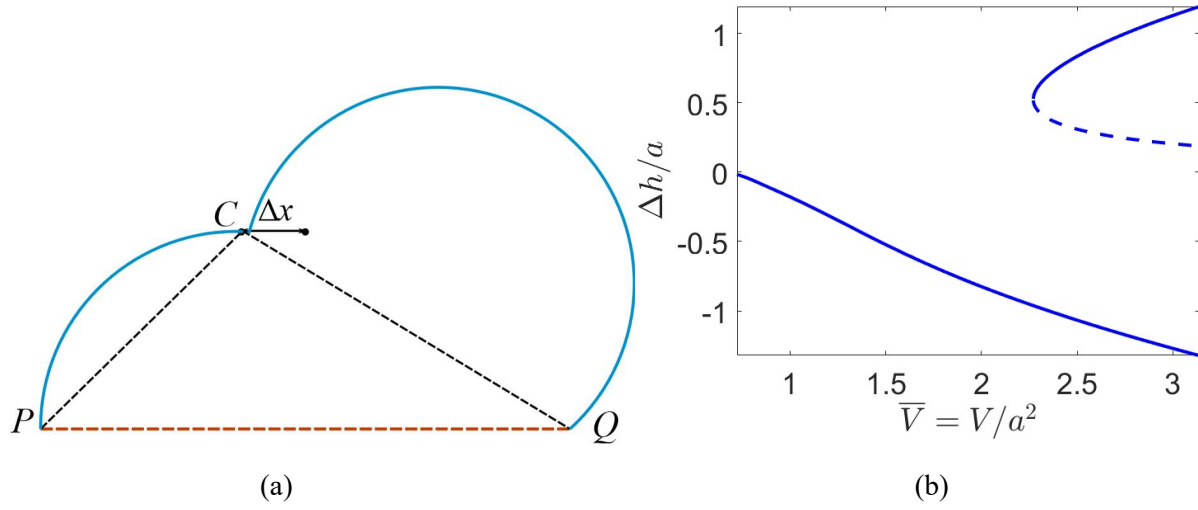
Figure 14 (a) schematics of membrane deformation with a finite indenter offset. (b)A bifurcation diagram for 2D line indentation with bias $\Delta x / a = 0.2$

In real system, even when there is no geometric imperfection, friction at the contact interface can delay the onset of bifurcation or require a larger disturbance for bifurcation to occur. To study the effects of friction, as shown in Figure 15, we fix a material point that is ΔS away from the center of membrane in the undeformed configuration to the line indenter (placed at the center, i.e., $\Delta x = 0$) in order to create an artificial offset. We then further inflate the membrane to a prescribed volume V_0. Since the contact point between the membrane and line indenter is specified rather than determined, the tensions within parts A and B are not necessarily equal and the resulting tension difference needs to be balanced by friction at the contact point (hence this type of perturbation does not apply to the frictionless case).
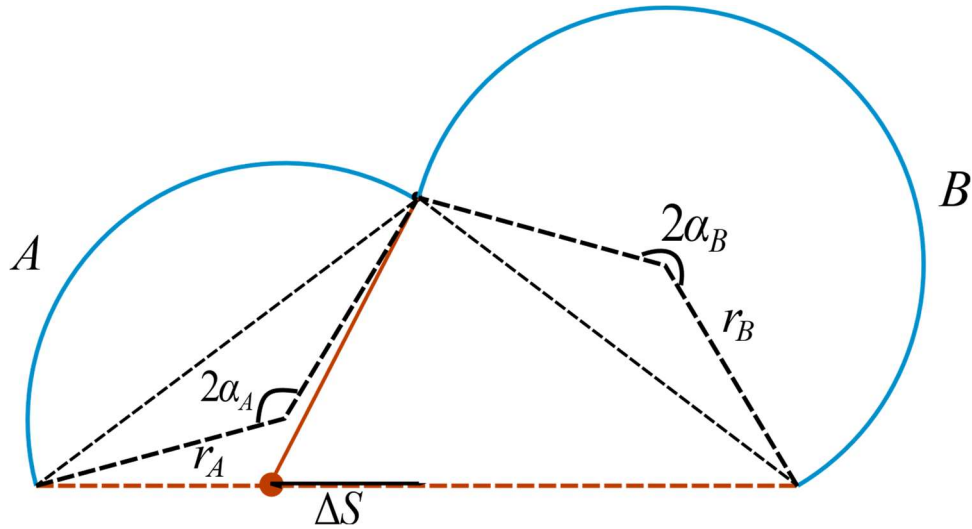

Figure 15 Schematic for deformed and undeformed membrane shapes. The material point that is ΔS away from the center of the membrane in the undeformed configuration is "fixed" onto the line indenter and the volume enclosed by the deformed membrane is prescribed.

The shapes of the arcs A and B can be determined by geometric constraints similar to Eq. (14), a volume constraint, and the fact that the pressures applied on part A and B are equal:

$$\overline{r}_A \sin \alpha_A = \frac{1}{2}\sqrt{1+\overline{d}^2}$$

$$\overline{r}_B \sin \alpha_B = \frac{1}{2}\sqrt{1+\overline{d}^2}$$

$$\frac{\overline{r}_A \alpha_A}{\lambda_A} - \frac{\overline{r}_B \alpha_B}{\lambda_B} = \Delta \overline{S}$$

$$\frac{\overline{r}_A \alpha_A}{\lambda_A} + \frac{\overline{r}_B \alpha_B}{\lambda_B} = 1 \tag{24}$$

$$\overline{r}_A^2 (\alpha_A - \sin \alpha_A \cos \alpha_A) + \overline{r}_B^2 (\alpha_B - \sin \alpha_B \cos \alpha_B) + \overline{d} = \overline{V}$$

$$\frac{\overline{T}_A}{\overline{r}_A} = \frac{\overline{T}_B}{\overline{r}_B}$$

where T is the membrane tension and related to the stretch ratio by $\overline{T} = \dfrac{T}{\mu h} = \lambda - \dfrac{1}{\lambda^3}$ (see Eq. (11)). Once we solve for the deformed shape, we further calculate half of total strain energy of the system as

$$\overline{E} = \frac{E}{\mu h a} = \left(\lambda_A^2 + \frac{1}{\lambda_A^2} - 2 \right) \frac{\alpha_A r_A}{\lambda_A} + \left(\lambda_B^2 + \frac{1}{\lambda_B^2} - 2 \right) \frac{\alpha_B r_B}{\lambda_B}. \tag{25}$$

(again, half of the energy is considered for simplicity of expression.) There are three extrema in Figure 16 (a) corresponding to three possible equilibrium solutions, among which the symmetric configuration ($\Delta \overline{S} = 0$) is a local energy maximum such that it is not a stable solution. Any perturbation will cause the system to jump to the local energy minima where there is a finite offset. The offset $\Delta \overline{S}$ can be converted to height difference $\Delta \overline{h}$ and, as a result, the local energy minima match with the solution branches in the bifurcation diagram, as shown in Figure 17 (a).
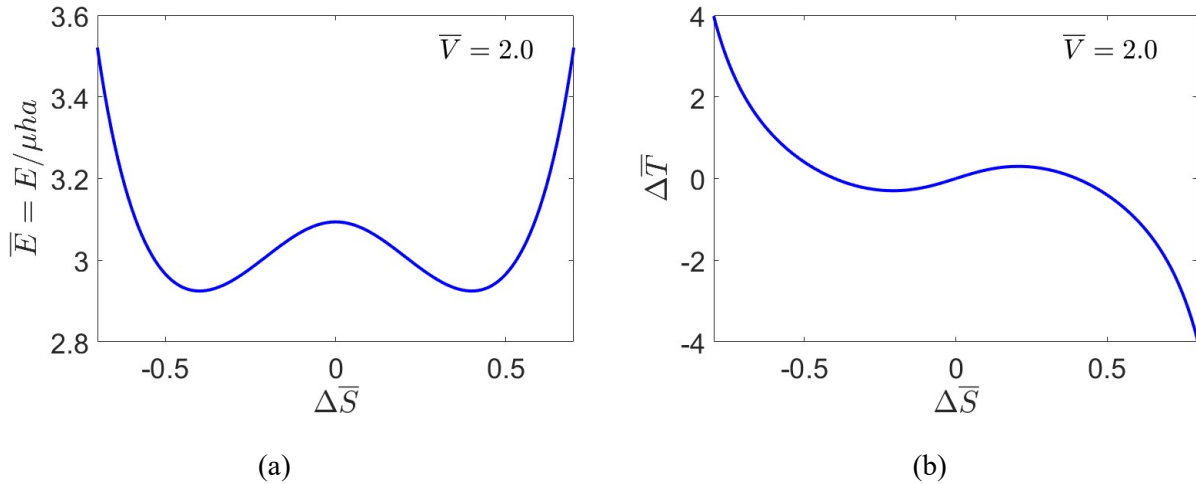

Figure 16 (a) Total energy of the system as a function of normalized offset when $\overline{V} = 2.0$. (b) Tension difference as a function of normalized offset when $\overline{V} = 2.0$.
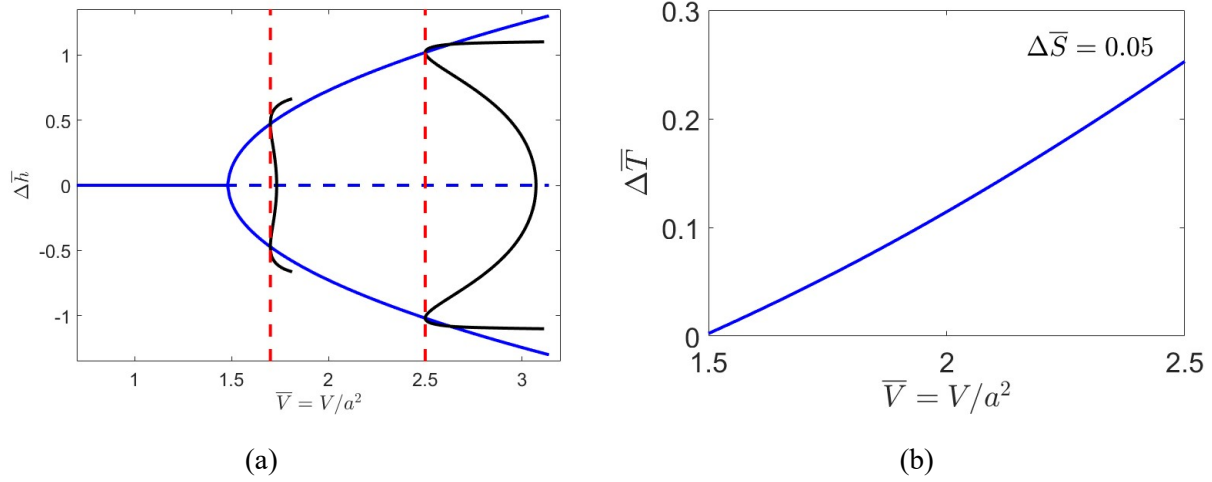
Figure 17 (a) The energy plot is transferred to a function of height difference and overlaid on the bifurcation diagram. The energy local minima match exactly the asymmetric equilibrium solution (b) Tension difference as a function of the normalized volume for a fixed offset.

The energetic force that drives the system to its local energy minima is essentially the tension difference between parts A and B. This force can also be visualized as the slope in the energy plot in Figure 16(a) and Figure 17(a), where we can intuitively see that, by increasing offset or by increasing volume, we effectively increase the tension difference. This is numerically verified by the results shown in Figure 16(b) and Figure 17(b).

In reality, friction can resist the tension difference and hold the membrane at a given offset to prevent bifurcation. We can either increase the offset or increase the volume to increase the tension difference to overcome the friction and drive the system to the bifurcated branch. Note that, if we increase volume to increase tension difference, the membrane will jump to the bifurcated branch once friction is no longer sufficient to hold the membrane. This is different from the smooth continuous bifurcation we see in the frictionless case.

6. Discussion and conclusions

For an inflated membrane indented by a rigid indenter, we find that there can be multiple equilibrium solutions that satisfy all equilibrium, constitutive, and kinematic constraints. We compute the total system potential energy for each solution and determine if and when one solution becomes energetically preferred. Our results show that a deformed membrane remains symmetric if the inflated volume is small. As a critical volume is reached, the membrane will bifurcate to an asymmetric shape that has lower total energy. At least for the 2-D scenario, most of our results are material model independent as long as the strain energy density function is monotonic. Using numerical methods, we are also able to consider different membrane and indenter geometries and find that, in general, a cylindrical indenter can trigger bifurcation more easily than spherical indenters and that larger indenters are more likely to induce bifurcation than smaller ones. We also demonstrate that friction can potentially delay the onset of bifurcation or require a larger bias for bifurcation to occur.

Our results suggest several considerations regarding practical applications. When soft robots navigate through complex environments, bifurcation is the preferred state for the soft chamber since we show that

the bifurcated asymmetric deformation mode can achieve the same volume with significantly less strain energy. Therefore, bifurcation can help avoid overstrain of soft robotic skin. One should be very careful regarding indenters that have a small or sharp head since the membrane tends to wrap around such indenters. Practically speaking, when a membrane is over-pressurized, the indenter can concentrate stresses and easily pierce through the membrane. Note that the lubrication of the membrane surface can also facilitate bifurcation. In addition to passive contact with the environment, it is also possible to add electrodes on both sides of the membrane to render it as a dielectric elastomer actuator (DEA). Related to this proposed implementation, tuning the voltage applied across full-coverage electrodes has been used in prior demonstrations to achieve different deformed shapes or snap through instabilities [37,38]. Here, we can also potentially leverage patterned-electrode DEAs to actively control the bifurcation behavior of an inflated balloon under indentation.

It should be noted that there are some limitations of our study that can be relaxed in the future. For example, we assume that the boundary of the inflated membrane is rigidly fixed. This is usually not the case for real soft robots and hence it is important to further investigate how the bifurcation behavior can be tuned using different boundary conditions. For simplicity, we also assumed the indenters to be rigid, which is not necessarily true for soft robotic or haptics applications. Furthermore, dynamic effects and viscoelastic material properties are potentially important for applications that require fast actuation. Studies of how to extend the physics explained in current work to specific applications will be done in the future.

Declaration of Competing Interest

References

1. Polygerinos P, Correll N, Morin SA, Mosadegh B, Onal CD, Petersen K, Cianchetti M, Tolley MT, Shepherd RF. 2017 Soft Robotics: Review of Fluid-Driven Intrinsically Soft Devices; Manufacturing, Sensing, Control, and Applications in Human-Robot Interaction. *Adv. Eng. Mater.* **19**. (doi:10.1002/adem.201700016)

2. Zhu M, Memar AH, Gupta A, Samad M, Agarwal P, Visell Y, Keller SJ, Colonnese N. 2020 PneuSleeve: In-fabric Multimodal Actuation and Sensing in a Soft, Compact, and Expressive Haptic Sleeve. In *Proceedings of the 2020 CHI Conference on Human Factors in Computing Systems*, pp. 1–12. New York, NY, USA: ACM. (doi:10.1145/3313831.3376333)

3. Young EM, Memar AH, Agarwal P, Colonnese N. 2019 Bellowband: A Pneumatic Wristband for Delivering Local Pressure and Vibration. In *2019 IEEE World Haptics Conference, WHC 2019*, pp. 55–60. Institute of Electrical and Electronics Engineers Inc. (doi:10.1109/WHC.2019.8816075)

4. Seedhouse E. 2015 Bigelow Expandable Activity Module. In *Bigelow Aerospace*, pp. 87–98. Springer International Publishing. (doi:10.1007/978-3-319-05197-0_5)

5. Huber JE, Fleck NA, Ashby MF. 1997 The selection of mechanical actuators based on performance indices. *Proc. R. Soc. London. Ser. A Math. Phys. Eng. Sci.* **453**, 2185–2205. (doi:10.1098/rspa.1997.0117)

6. Pikul JH, Li S, Bai H, Hanlon RT, Cohen I, Shepherd RF. 2017 Stretchable surfaces with programmable 3D texture morphing for synthetic camouflaging skins. *Science (80-.).* **358**, 210–214. (doi:10.1126/science.aan5627)

7. Hawkes EW, Blumenschein LH, Greer JD, Okamura AM. 2017 A soft robot that navigates its environment through growth. *Sci. Robot.* **2**. (doi:10.1126/scirobotics.aan3028)

8. Shepherd RF, Ilievski F, Choi W, Morin SA, Stokes AA, Mazzeo AD, Chen X, Wang M, Whitesides GM. 2011 Multigait soft robot. *Proc. Natl. Acad. Sci. U. S. A.* **108**, 20400–20403. (doi:10.1073/pnas.1116564108)

9. Comer RL, Levy S. 1963 Deflections of an inflated circular-cylindrical cantilever beam. *AIAA J.* **1**, 1652–1655. (doi:10.2514/3.1873)

10. Rothemund P, Ainla A, Belding L, Preston DJ, Kurihara S, Suo Z, Whitesides GM. 2018 A soft, bistable valve for autonomous control of soft actuators. *Sci. Robot.* **3**, eaar7986. (doi:10.1126/scirobotics.aar7986)

11. Gorissen B, Melancon D, Vasios N, Torbati M, Bertoldi K. 2020 Inflatable soft jumper inspired by shell snapping. *Sci. Robot* **5**, 1967. (doi:10.1126/scirobotics.abb1967)

12. Russo MJ, Steen PH. 1986 Instability of rotund capillary bridges to general disturbances: Experiment and theory. *J. Colloid Interface Sci.* **113**, 154–163. (doi:10.1016/0021-9797(86)90215-8)

13. Liu T, Xu X, Nadermann N, He Z, Jagota A, Hui CY. 2017 Interaction of Droplets Separated by an Elastic Film. *Langmuir* **33**, 75–81. (doi:10.1021/acs.langmuir.6b03600)

14. Wang T, Xu F, Huo Y, Potier-Ferry M. 2018 Snap-through instabilities of pressurized balloons: Pear-shaped bifurcation and localized bulging. *Int. J. Non. Linear. Mech.* **98**, 137–144. (doi:10.1016/j.ijnonlinmec.2017.10.017)

15. Fu YB, Xie YX. 2014 Stability of pear-shaped configurations bifurcated from a pressurized spherical balloon. *J. Mech. Phys. Solids* **68**, 33–44. (doi:10.1016/j.jmps.2014.03.007)

16. Zhou Y, Nordmark A, Eriksson A. 2015 Instability of thin circular membranes subjected to hydro-static loads. *Int. J. Non. Linear. Mech.* **76**, 144–153. (doi:10.1016/j.ijnonlinmec.2015.06.010)

17. Debotton G, Bustamante R, Dorfmann A. 2013 Axisymmetric bifurcations of thick spherical shells under inflation and compression. *Int. J. Solids Struct.* **50**, 403–413. (doi:10.1016/j.ijsolstr.2012.10.004)

18. Eriksson A, Nordmark A. 2012 Instability of hyper-elastic balloon-shaped space membranes under pressure loads. *Comput. Methods Appl. Mech. Eng.* **237**–**240**, 118–129. (doi:10.1016/j.cma.2012.05.012)

19. Tamadapu G, Dasgupta A. 2014 Finite inflation of a hyperelastic toroidal membrane over a cylindrical rim. *Int. J. Solids Struct.* **51**, 430–439. (doi:10.1016/j.ijsolstr.2013.10.016)

20. Steigmann DJ, Pipkin AC. 1989 Wrinkling of pressurized membranes. *J. Appl. Mech. Trans.*

ASME **56**, 624–628. (doi:10.1115/1.3176137)

21. Vella D, Huang J, Menon N, Russell TP, Davidovitch B. 2015 Indentation of ultrathin elastic films and the emergence of asymptotic isometry. *Phys. Rev. Lett.* **114**, 014301. (doi:10.1103/PhysRevLett.114.014301)

22. Patil A, Nordmark A, Eriksson A. 2016 Instabilities of wrinkled membranes with pressure loadings. *J. Mech. Phys. Solids* **94**, 298–315. (doi:10.1016/j.jmps.2016.05.014)

23. Long R, Shull KR, Hui C-Y. 2010 Large deformation adhesive contact mechanics of circular membranes with a flat rigid substrate. *J. Mech. Phys. Solids* **58**, 1225–1242. (doi:10.1016/J.JMPS.2010.06.007)

24. Srivastava A, Hui C-Y. 2013 Large deformation contact mechanics of long rectangular membranes. I. Adhesionless contact. *Proc. R. Soc. A Math. Phys. Eng. Sci.* **469**, 20130424–20130424. (doi:10.1098/rspa.2013.0424)

25. Patil A, Dasgupta A, Eriksson A. 2015 Contact mechanics of a circular membrane inflated against a deformable substrate. *Int. J. Solids Struct.* **67–68**, 250–262. (doi:10.1016/j.ijsolstr.2015.04.025)

26. Liu MX, Wang CG, Li XD. 2018 Rigid-flexible contact analysis of an inflated membrane balloon with various contact conditions. *Int. J. Solids Struct.* **144–145**, 218–229. (doi:10.1016/j.ijsolstr.2018.05.004)

27. Chandler TGJ, Vella D. 2020 Indentation of suspended two-dimensional solids: The signatures of geometrical and material nonlinearity. *J. Mech. Phys. Solids* , 104109. (doi:10.1016/j.jmps.2020.104109)

28. Vella D, Ajdari A, Vaziri A, Boudaoud A. 2012 The indentation of pressurized elastic shells: From polymeric capsules to yeast cells. *J. R. Soc. Interface* **9**, 448–455. (doi:10.1098/rsif.2011.0352)

29. Vella D, Ajdari A, Vaziri A, Boudaoud A. 2012 Indentation of ellipsoidal and cylindrical elastic shells. *Phys. Rev. Lett.* **109**, 144302. (doi:10.1103/PhysRevLett.109.144302)

30. Hutchinson JW, Thompson JMT. 2017 Nonlinear Buckling Interaction for Spherical Shells Subject to Pressure and Probing Forces. *J. Appl. Mech. Trans. ASME* **84**. (doi:10.1115/1.4036355)

31. Zhou Y, Nordmark A, Eriksson A. 2017 Multi-parametric stability investigation for thin spherical membranes with contacts. *Int. J. Mech. Sci.* **131–132**, 334–344. (doi:10.1016/j.ijmecsci.2017.07.011)

32. Green A. 1970 *Large elastic deformations*. 2nd ed. Oxford: Univ. Press.

33. Oden JT, Sato T. 1967 Finite strains and displacements of elastic membranes by the finite element method. *Int. J. Solids Struct.* **3**, 471–488. (doi:10.1016/0020-7683(67)90002-9)

34. Libai A, Simmonds JG. 1998 *The Nonlinear Theory of Elastic Shells*. Cambridge University Press. (doi:10.1017/cbo9780511574511)

35. Soares RM, Amaral PFT, Silva FMA, Gonçalves PB. 2020 Nonlinear breathing motions and instabilities of a pressure-loaded spherical hyperelastic membrane. *Nonlinear Dyn.* **99**, 351–372. (doi:10.1007/s11071-019-04855-4)

36. Deris AHA, Nadler B. 2015 Modeling the indentation and puncturing of inflated elastic membranes by rigid indenters. *Int. J. Non. Linear. Mech.* **69**, 29–36. (doi:10.1016/j.ijnonlinmec.2014.10.020)

37.   Wang F, Yuan C, Lu T, Wang TJ. 2017 Anomalous bulging behaviors of a dielectric elastomer balloon under internal pressure and electric actuation. *J. Mech. Phys. Solids* **102**, 1–16. (doi:10.1016/j.jmps.2017.01.021)

38.   Li T, Keplinger C, Baumgartner R, Bauer S, Yang W, Suo Z. 2013 Giant voltage-induced deformation in dielectric elastomers near the verge of snap-through instability. *J. Mech. Phys. Solids* **61**, 611–628. (doi:10.1016/j.jmps.2012.09.006)